Check for updates

ARTICLE   OPEN

Experimental observation of spin−split energy dispersion in high-mobility single-layer graphene/WSe$_2$ heterostructures

Priya Tiwari[1], Mohit Kumar Jat[1], Adithi Udupa[2], Deepa S. Narang[1], Kenji Watanabe [iD][3], Takashi Taniguchi [iD][4], Diptiman Sen[1,2] and Aveek Bid [iD][1] ✉

Proximity-induced spin–orbit coupling in graphene has led to the observation of intriguing phenomena like time-reversal invariant $\mathbb{Z}_2$ topological phase and spin-orbital filtering effects. An understanding of the effect of spin–orbit coupling on the band structure of graphene is essential if these exciting observations are to be transformed into real-world applications. In this research article, we report the experimental determination of the band structure of single-layer graphene (SLG) in the presence of strong proximity-induced spin–orbit coupling. We achieve this in high-mobility hexagonal boron nitride (hBN)-encapsulated SLG/WSe$_2$ heterostructures through measurements of quantum oscillations. We observe clear spin-splitting of the graphene bands along with a substantial increase in the Fermi velocity. Using a theoretical model with realistic parameters to fit our experimental data, we uncover evidence of a band gap opening and band inversion in the SLG. Further, we establish that the deviation of the low-energy band structure from pristine SLG is determined primarily by the valley-Zeeman SOC and Rashba SOC, with the Kane–Mele SOC being inconsequential. Despite robust theoretical predictions and observations of band-splitting, a quantitative measure of the spin-splitting of the valence and the conduction bands and the consequent low-energy dispersion relation in SLG was missing— our combined experimental and theoretical study fills this lacuna.

npj 2D Materials and Applications (2022)6:68 ; https://doi.org/10.1038/s41699-022-00348-y

INTRODUCTION

Graphene has attracted much attention due to a plethora of remarkable electronic properties like Dirac energy dispersion, relativistic effects, half-integer quantum Hall effect, and Klein tunneling. Additionally, its van der Waals heterostructures with other 2-dimensional materials[1–4] host several single-particle and emergent correlated states that are topologically non-trivial[5–8]. The ability to precisely transfer and align these atomically thin planar structures into high-quality heterostructures promises outstanding opportunities for both fundamental and applied research[9–11]. This has made theoretical and experimental studies of several aspects of graphene-based van der Waals heterostructures of great contemporary interest[8,10–19].

With a long spin-relaxation length of several μm at room temperature, graphene appears a perfect base for low-power spintronics devices[20,21]. However, its extremely weak intrinsic spin–orbit coupling (SOC) strength makes spin manipulation challenging. Decorating the surface of graphene with heavy atoms (such as topological nanoparticles)[7,22] or weak hydrogenation of graphene[23] improves the SOC in graphene at the cost of introducing disorder and reducing the graphene's mobility. An alternate technique is interfacing graphene with two-dimensional transition metal dichalcogenides (TMDC) having a high SOC[11,16,19,21,24–35].

Before one conceives increasingly complex graphene/TMDC heterostructures and considers their potential applications, it is imperative to understand the impact of the proximity of TMDC on the electronic properties of graphene. Prominent amongst these are the breaking of inversion symmetry, breaking of sublattice symmetry, and hybridization of the d-orbitals of the heavy element in TMDC with the p-orbitals of SLG, leading to strong SOC in SLG. This proximity-induced SOC in SLG has three primary components, all of which contribute to spin splitting of the bands—(i) valley-Zeeman (also called Ising) term, which couples the spin and valley degrees of freedom, (ii) Kane–Mele term[36,37], which couples the spin, valley and sublattice components and opens a topological gap at the Dirac point[18,38], and (iii) Rashba term[39] which couples the spin and sublattice components.

In the presence of a strong Ising SOC, the electronic band dispersion of graphene is predicted to be spin–split[17,24,39–42], as was observed recently in bilayer graphene/WSe$_2$ heterostructures[10,43]. Consequences of this induced SOC include the appearance of helical edge modes and quantized conductance in the absence of a magnetic field in bilayer graphene[5] and of weak antilocalization[19], and Hanle precession in SLG[27,28,44,44–48]. Despite these advances, a quantitative study of the effect of a strong SOC on the electronic energy band dispersion of SLG is lacking.

In this research article, we report the results of our studies of quantum oscillations in high-mobility heterostructures of SLG and trilayer WSe$_2$. Careful analysis of the oscillation frequencies shows spin-splitting of the order of ~5 meV for both the valence band (VB) and the conduction band (CB). We find that the bands remain linear down to at least 70 meV (corresponding to $n \sim 2 \times 10^{11} \mathrm{cm}^{-2}$). Close to zero energy, the lower energy branches of the CB and the VB overlap, leading to band inversion and opening of a band gap in the energy dispersion of SLG. We fit our data using a theoretical model that establishes that, to the zeroth order, the magnitude of the spin-splitting of the bands and that of the band gap are determined by only the valley-Zeeman and Rashba spin–orbit interactions.

[1]Department of Physics, Indian Institute of Science, Bangalore 560012, India. [2]Centre for High Energy Physics, Indian Institute of Science, Bangalore 560012, India. [3]Research Center for Functional Materials, National Institute for Materials Science, 1-1 Namiki, Tsukuba 305-0044, Japan. [4]International Center for Materials Nanoarchitectonics, National Institute for Materials Science, 1-1 Namiki, Tsukuba 305-0044, Japan. ✉email: aveek@iisc.ac.in
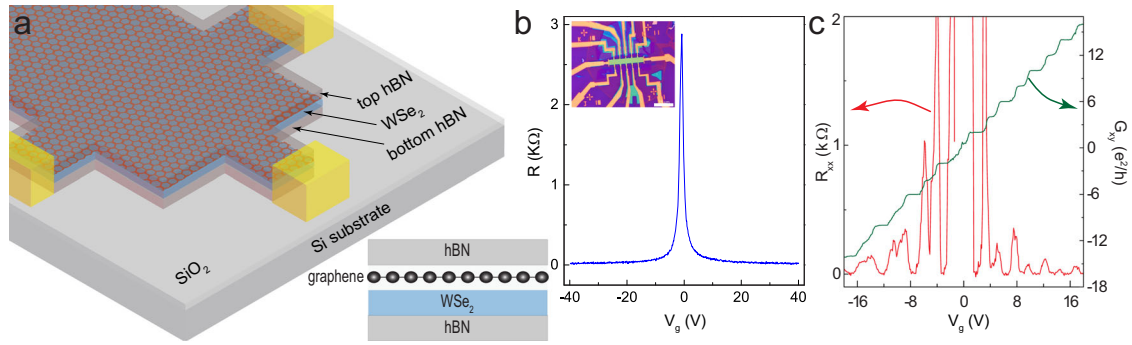
npj

Fig. 1 Transport measurements in hBN encapsulated SLG/WSe₂ heterostructures. a A schematic of the device. The bottom right corner shows the sequence of all the layers of the heterostructure. b Four-probe resistance of the device plotted as a function of the back-gate voltage V_{bg}; the data were collected at 20 mK. An optical image of the device is shown in the inset. The scale bar in the figure is 15 μm. c Plots of longitudinal resistance R_{xx} (left-axis) and the Hall conductance G_{xy} (right-axis) versus V_{bg} in the quantum Hall regime. The measurements were done at 20 mK in the presence of a 3 T perpendicular magnetic field.

RESULTS

Experimental observations

Heterostructures of single-layer graphene and trilayer WSe₂, encapsulated by hexagonal boron nitride (hBN) (see device schematic Fig. 1a) of thickness ~20–30 nm, were fabricated using dry transfer technique[49,50]. One-dimensional Cr/Au electrical contacts were created by standard nanofabrication techniques—note that this method completely evades contacting the WSe₂ thus avoiding parallel channel transport (see Supplementary Information for details). Electrical transport measurements were performed using a low-frequency ac lock-in technique in a dilution refrigerator at the base temperature of 20 mK unless specified otherwise. Multiple devices of SLG/WSe₂ were studied, and the data from all of them were qualitatively very similar. All the data presented here are from a device labeled B9S6. The data for two other similar devices are presented in the Supplementary Information. The extracted impurity density from the four-probe resistance of the device as a function of gate voltage (see Fig. 1b) was ~2.2×10^{10} cm^{-2}, and the mobility was ~ 140,000 cm²V^{-1}s^{-1}. The four-probe resistance response as a function of the gate voltage were identical for different measurement configurations (see Supplementary Information), indicating that the fabricated device is spatially homogeneous. Figure 1c shows the quantum Hall data at 3 T – the presence of plateaus at $v = \pm 2, \pm 6, \pm 10$ confirms it as SLG. Along with the signature plateaus of SLG, one can see a few of the broken symmetry states appearing already at 3 T, confirming it to be a high-quality device.

Representative data of the Shubnikov-de Haas (SdH) oscillations measured at 20 mK are plotted in Fig. 2a. In addition to the expected decay of the amplitude of the oscillations with increasing 1/B, we observe the presence of beating, implying two closely spaced frequencies. The fast Fourier transforms (FFT) of the data Fig. 2b show that this indeed is the case. We find similar splitting in the SdH oscillation frequency in all the SLG/WSe₂ devices studied by us—the data for two additional similar devices are presented in the Supplementary Information. There may be a legitimate concern that the observed beating can be caused by device inhomogeneities which lead to different charge carrier density in different regions of the graphene channel. We rule out this artifact from measurements of the four-probe resistance and SdH oscillations in multiple contact configurations—we find that the data are identical in each case (see Supplementary Information).

Recall that the SdH oscillation frequency, B_F is directly related to the cross-sectional area $A(\mathbf{k})$ at the Fermi energy by the relation $B_F = \hbar A(\mathbf{k})/2\pi e$[51]. For an isotropic dispersion in which the Fermi energy E_F is a function of $k_F = \sqrt{k_x^2 + k_y^2}$ (where (k_x, k_y) are defined with respect to one of the Dirac points, K or K', of the SLG), the
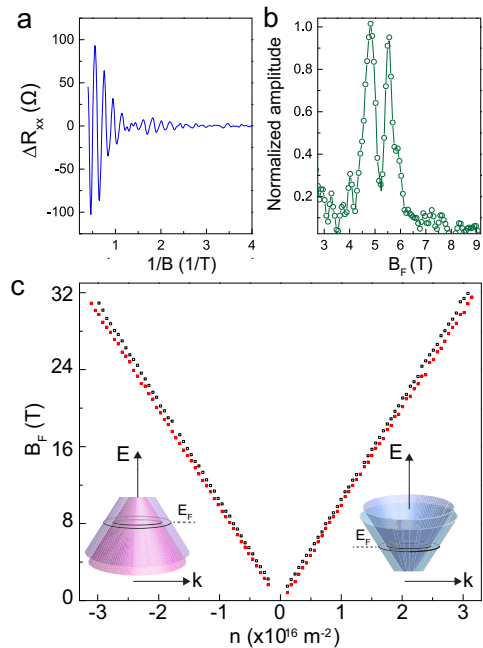

Fig. 2 Shubnikov-de Haas(SdH) oscillations. a Plot of the Shubnikov-de Haas oscillations measured at $V_{bg} = -9$ V and $T = 20$ mK. b The corresponding FFT spectra showing two distinct peaks. c Charge carrier density (n) dependence of the frequency of SdH oscillations. The inset shows the schematics of the spin split conduction and valance bands.

cross-sectional area of the Fermi surface is given by $A(\mathbf{k}) = \pi k_F^2$. Figure 2c shows the charge carrier density (n) dependence of B_F. The appearance of two closely spaced frequencies at all n (or E_F) implies that for each value of the Fermi energy, there are two distinct values of k_F. This is a direct proof of the energy splitting of both the CB and the VB of the SLG.

From the temperature dependence of the amplitude of the SdH oscillations (Fig. 3), we extracted the effective charge carrier mass m^*, using the the Lifshitz–Kosevich relation[52,53]:

$$\frac{\Delta R_{xx}}{R_0} \propto \frac{2\pi^2 k_B T m^*/\hbar e B}{\sinh(2\pi^2 k_B T m^*/\hbar e B)},$$ (1)

Here, R_0 the longitudinal resistivity at B = 0. On fitting the effective mass m^* versus n using the relation $m^* = \hbar(\sqrt{\pi}/v_F)n^a$[54] (see Supplementary Information), we obtain $a = 0.5 \pm 0.02$ and Fermi

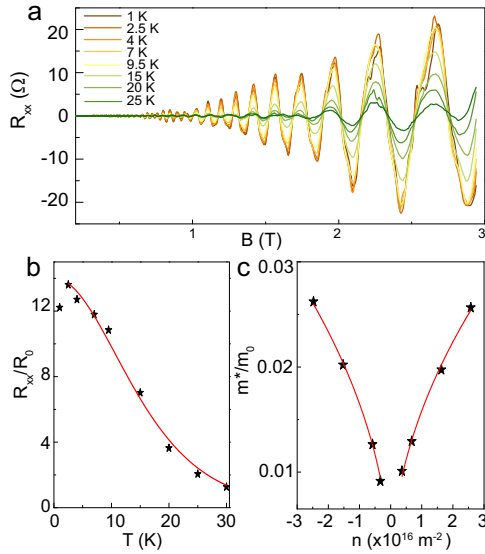**Fig. 3 Temperature dependent SdH oscillations and effective mass extraction. a** SdH oscillations for different temperatures measured at $V_{bg} = 25$ V. **b** The normalized amplitude of the SdH oscillations as a function of temperature (black stars). The solid red line is the fit to Eq. (1) used to extract the effective mass. **c** Plot of the effective mass m^* versus the charge carrier density n (black stars). The solid red curve is the fit used to extract the relation between m^* and n.
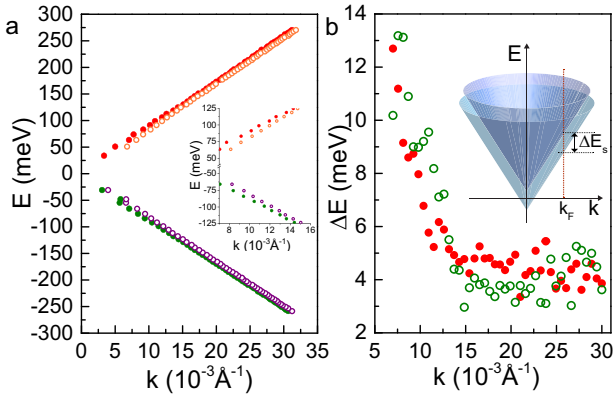

Fig. 4 Experimentally obtained dispersion relation. a Dispersion relation for SLG on WSe$_2$ as extracted from our SdH measurements. The inset shows the zoomed-in plot near the Dirac point. **b** Plot of the magnitude of the energy difference between the two spin–split bands, ΔE_s versus k for the valence band (green open circles) and the conduction band (red filled circles). The inset shows a schematic of the band-splitting in the CB— ΔE_s is the spin-splitting at k_F.

velocity $v_F = 1.29 \pm 0.04 \times 10^6$ ms^{-1}. The value of a being 0.5 establishes the dispersion relation between energy and momentum in SLG on WSe$_2$ to be linear[51].

Figure 4a are the resultant plots of E versus k for both CB and the VB from our experimental data. Note that our experimental data extends down to ≈ 30 meV (corresponding to $n \approx 3.9 \times 10^{10}$ cm^{-2}). Below this number density, the SdH oscillations are not resolvable – presumably due to the dominance of charge puddles on the electrical transport of SLG in this energy range.

We observe that, on extrapolating the $E - k$ plots to $E = 0$, the low-energy branches of the spin–split bands of both the CB and the VB bands enclose a finite area in the k-space at $E = 0$. This leads us to expect that there will be an overlap between the lower branches of the CB and VB, ultimately leading to band inversion

near the K (and K') points. A verification of this assertion requires further measurements in extremely high quality devices that will allow measurements of SdH oscillations near $E = 0$.

To summarize our experimental observations, we have quantified the spin-splitting of the energy bands in SLG in proximity to WSe$_2$ and mapped out the dispersion relation of the spin–split bands of SLG. We find that till a certain energy, the dispersion remains linear; below this energy scale, we observe a deviation from linearity.

Theoretical calculations

Using the experimental data, we fit a theoretical model to obtain the dispersion relation close to the Dirac points. The continuum Hamiltonian near the Dirac points for SLG with WSe$_2$ has the following terms (see, for instance, ref. [39]):

$$H = \hbar v_F(\eta k_x \sigma_x + k_y \sigma_y) + \Delta \sigma_z + \lambda_{KM} \eta S_z \sigma_z + \lambda_{VZ} \eta S_z + \lambda_R(\eta S_y \sigma_x - S_x \sigma_y)$$
$$+ \frac{\sqrt{3}a}{2}[\lambda_{PIA}^A(\sigma_z + \sigma_0) + \lambda_{PIA}^B(\sigma_z - \sigma_0)](k_x S_y - k_y S_x)$$

$$(2)$$

In Eq. (2), the Pauli matrices σ_i and the S_i represent the sublattice and spin degrees of freedom, respectively. The first term denotes the linear dispersion near the Dirac points, where v_F is the Fermi velocity, k_x and k_y are the momenta with respect to the Dirac point, and $\eta = \pm 1$ denotes the valleys K (K') respectively (We note that $\hbar v_F = 3ta/2$, where t is the nearest-neighbor hopping amplitude and the nearest neighbor carbon carbon distance a is 1.42 Å). The second term represents a sublattice potential of strength Δ. We have considered the four possible spin–orbit couplings: (i) Kane–Mele SOC with strength λ_{KM}, (ii) valley-Zeeman SOC with strength λ_{VZ}, (iii) Rashba SOC with strength λ_R, and (iv) pseudo-spin asymmetric SOC with strengths λ_{PIA}^A and λ_{PIA}^B for sublattices A and B respectively.

Since this Hamiltonian results in the same dispersion at both the valleys, we only consider the case $\eta = +1$ (K point). The Hamiltonian in Eq. (2) is invariant under a simultaneous rotation of (k_x, k_y), (σ_x, σ_y) and (S_x, S_y) by the same angle; this implies that the dispersion is isotropic in momentum space, and it is sufficient to take $k_x = k$ and $k_y = 0$. The data for the four bands shown in Fig. 4a are fitted to the Hamiltonian with $t, \Delta, \lambda_{KM}, \lambda_{VZ}$ and λ_R as the fit parameters. The best fit gives $t = 3979.10 \pm 3.99$ meV implying a large Fermi velocity in this device of 1.286×10^6 ms^{-1} (compared to about 0.86×10^6 ms^{-1} in pristine SLG[55]). The parameters in the Hamiltonian which give the spin–split band gap in both conduction and valence bands are λ_{VZ} and λ_R. We find that the best fit gives the values of λ_{VZ} and λ_R to lie on a circle of radius 2.51 meV, such that

$$\lambda_{VZ} = 2.51 \cos\theta \text{ meV}, \quad \text{and} \quad \lambda_R = 2.51 \sin\theta \text{ meV}. \quad (3)$$

where θ can take any value from 0 to 2π, and $\Delta = \lambda_{KM} = 0$. Eq. (3) can be understood by looking at the first-order perturbative effect of the valley-Zeeman and Rashba terms in the Hamiltonian. Taking $H_0 = \hbar v_F k \sigma_x$ and the perturbation $V = \lambda_{VZ} S_z + \lambda_R(S_y \sigma_x - S_x \sigma_y)$, we find that the zeroth order spin-degenerate dispersion $E_0 = \pm \hbar v_F k$ in the positive and negative energy bands receives first-order corrections given by

$$E_{1,\pm} = \pm \sqrt{\lambda_{VZ}^2 + \lambda_R^2} = \pm 2.51 \text{ meV} \quad (4)$$

for both the bands, thus giving the general relation in Eq. (3). This gives a gap equal to twice 2.51 meV which fits the experimentally observed value of ~ 5 meV. The two extreme cases are given by $\theta = 0$ with only valley-Zeeman SOC and $\theta = \pi/2$ with only Rashba SOC.

The overall magnitude of effective SOC of 2.51 meV agrees well with previous reports[18,19,39,48].

The band dispersion for higher energies ($E > 5$ meV) remains unaffected for any combination of λ_{VZ} and λ_R which satisfies
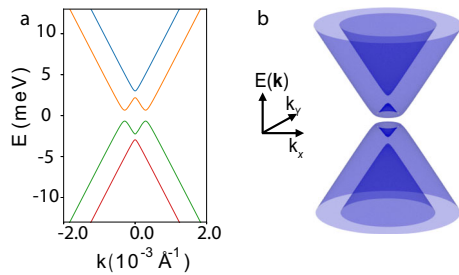
Fig. 5 Theoretically calculated dispersion relation. a A 2D plot of the energy dispersion relation calculated with $v_F = 1.286 \times 10^6 ms^{-1}$, and $\theta = 13°$ ($\lambda_{VZ} \simeq \pm 2.45$ meV and $\lambda_R = \pm 0.56$ meV). The value of λ_R is taken from ref. [39]. The value of λ_{VZ} comes from fitting the experimental spin split band gap energy. Further, the other parameters in this graph have been set as follows: $\Delta = 0.54$ meV, $\lambda_{KM} = 0.03$ meV, $\lambda_{PIA}^A = -2.69$ meV and $\lambda_{PIA}^B = -2.54$ meV. **b** The 3D dispersion of this model for the same set of parameters as in (**a**).

$\sqrt{\lambda_{VZ}^2 + \lambda_R^2} = 2.51$ meV. However, the relative magnitudes of λ_{VZ} and λ_R modifies the lower energy band dispersion ($E < 5$ meV) – a region inaccessible in our experiments. To evaluate the value of λ_{VZ} and λ_R explicitly, one needs the value of the band gap at $E = 0$. As is well known, the presence of finite impurity density ($n_0 \approx 2.2 \times 10^{10}$ cm^{-2} for this device) leads to the dominance of charge puddles on the electrical transport of SLG at the Dirac point making it extremely difficult to make an accurate estimate of such a small energy gap. In the absence of such information, we take the theoretically predicted value of $\lambda_R = 0.56$ meV[39] which corresponds to $\theta = 13°$ in Eq. (3). This yields the strength of the valley-Zeeman term to be $\lambda_{VZ} = 2.45$ meV and a maximum expected band gap of 3.3 meV for $\lambda_{so} \sim 2.51$ meV. The resulting dispersion is plotted in Fig. 5a. In generating this plot, we have used $\Delta = 0.54$ meV, $\lambda_{km} = 0.03$ meV, $\lambda_{PIA}^A = -2.69$ meV and $\lambda_{PIA}^B = -2.54$ meV[39]. Figure 5b further shows the 3-dimensional plot of the energy dispersion for this model.

DISCUSSIONS

Coming to the role of the magnetic field in the extracted energy dispersion relation, the SdH oscillations were studied at a magnetic field of the order of 1 T. This field gives a very small Zeeman energy of the order of 0.08meV in the energy. Since the experimental data points are quite far from $E = 0$, we can ignore the magnetic field effect in the Hamiltonian. Further, the fitting does not give us the values of Δ, λ_{KM}, λ_{PIA}^A, and λ_{PIA}^B with any certainty. While the *PIA* terms do not alter the dispersion in our region of interest, the other two parameters, Δ and λ_{KM} will open up a gap at the two values of the energy lying at $k = 0$. The effect of the Kane–Mele term in this model has been further discussed in the Supplementary Information. However, we note that the presence of Δ, λ_{KM}, λ_{PIA}^A and λ_{PIA}^B does not alter the spin–split band gap of 5 meV observed between the bands away from zero energy.

All previous theoretical and experimental studies note that the valley-Zeeman λ_{VZ} and the Rashba λ_R are the major spin–orbit coupling (SOC) terms for graphene/TMDs[18,19,39,48]. These two terms by themselves give a constant energy gap between the spin–split bands. The other relevant spin–orbit coupling terms are λ_{PIA} and λ_{KM}. The λ_{PIA} terms are negligibly small and do not alter the band dispersion in the region of interest. On the other hand, we find that including a very large λ_{KM} and Δ terms ~20 meV in the standard theoretical models can give a dispersion where the energy gap between the two spin–split bands increases as one approaches the Dirac point. However, such large λ_{KM} and Δ might not be reasonable and have not been reported to date. To the

best of our knowledge, there is no consistent theoretical understanding of the increase in energy gap between the spin–split bands on approaching the Dirac point; we leave this as an open question to be explored in near future.

Finally, a comment on the relative magnitudes of λ_{VZ} and λ_R: The spin relaxation mechanism in graphene/TMDC heterostructures is extraordinary. It relies on intervalley scattering and can only occur in materials with spin-valley coupling. In such systems, the lifetime τ and relaxation length λ of spins pointing parallel to the graphene plane ($\tau_s^\parallel$, $\lambda_s^\parallel$) can be markedly different from those of spins pointing out of the graphene plane ($\tau_s^\perp$, $\lambda_s^\perp$). Realistic modeling of experimental studies indicate that the spin lifetime anisotropy ratio $\zeta = \tau_s^\parallel / \tau_s^\perp = (\lambda_s^\perp / \lambda_s^\parallel)^2$ can be as large as a few hundred in the presence of intervalley scattering[41,44,47]. Recall that the λ_{VZ} provides an out-of-plane spin–orbit field and affects the in-plane spin relaxation time, $\tau_s^\parallel$. On the other hand, λ_R generates an in-plane spin–orbit field and is relevant for determining $\tau_s^\perp$[47]. The large spin lifetime anisotropy ratio ($\tau_s^\parallel / \tau_s^\perp \gg 1$) seen both from experiments and theory[41,44,47] show that the value of λ_{VZ} can indeed be significantly larger as compared to λ_R.

In conclusion, we have experimentally determined the band structure of single-layer graphene in the presence of proximity-induced SOC. We find both the VB and the CB spin–split with a spin-energy gap of ~5 meV; the splitting increases as one approaches the Dirac point. There are strong indications of overlap of the lower energy branches of the conduction and the valence bands. We also provide precise values of the spin splitting energy, the Fermi velocity and the effective mass of charge carriers in graphene/WSe$_2$ hetrostructures. Theoretical modeling of the data establishes that the band dispersion near the Dirac point and the magnitude of the spin-splitting are determined primarily by large valley-Zeeman (Ising) SOC and small Rashba SOC. Our work raises the strong possibility that in this system, the transport properties near the Dirac point are dominated by charge carriers of a single spin component, making this system a potential platform for realizing spin-dependent transport phenomena, such as quantum spin-Hall and spin-Zeeman Hall effects.

METHODS

Device fabrication

The SLG, WSe$_2$, and hBN flakes were obtained by mechanical exfoliation on SiO$_2$/Si wafer using scotch tape from the corresponding bulk crystals. The thickness of the flakes was verified from Raman spectroscopy. Heterostructures of SLG and WSe$_2$, encapsulated by single-crystalline hBN flakes of thickness ~ 20–30 nm was fabricated by dry transfer technique using a home-built transfer set-up consisting of high-precision XYZ-manipulators. The heterostructure was then annealed at 250 °C for 3 h. Electron beam lithography followed by reactive ion etching (where the mixture of CHF$_3$ and O$_2$ gas were used with flow rates of 40 sccm and 4 sscm, respectively, at a temperature of 25 °C at the RF power of 60 W) was used to define the edge contacts. The electrical contacts were fabricated by depositing Cr/Au (5/60 nm) followed by lift-off in hot acetone and IPA.

Measurements

All electrical transport measurements were performed using a low-frequency AC lock-in technique in a dilution refrigerator (capable of attaining a lowest temperature of 20 mK and maximum magnetic field of 16 T).

DATA AVAILABILITY

The authors declare that the data supports the findings of this study are available within the main text and its Supplementary Information. Other relevant data are available from the corresponding author upon reasonable request.

REFERENCES

1. Geim, A. K. & Grigorieva, I. V. Van der waals heterostructures. *Nature* **499**, 419–425 (2013).
2. Lotsch, B. V. Vertical 2d heterostructures. *Ann. Rev. Mater. Res.* **45**, 85–109 (2015).
3. Wang, H. et al. Two-dimensional heterostructures: fabrication, characterization, and application. *Nanoscale* **6**, 12250–12272 (2014).
4. Zhou, X. et al. 2d layered material-based van der waals heterostructures for optoelectronics. *Adv. Funct. Mater.* **28**, 1706587 (2018).
5. Tiwari, P., Srivastav, S. K., Ray, S., Das, T. & Bid, A. Observation of time-reversal invariant helical edge-modes in bilayer graphene/wse2 heterostructure. *ACS Nano* **15**, 916–922 (2020).
6. Cao, Y. et al. Unconventional superconductivity in magic-angle graphene superlattices. *Nature* **556**, 43–50 (2018).
7. Hatsuda, K. et al. Evidence for a quantum spin hall phase in graphene decorated with bi2te3 nanoparticles. *Sci. Adv.* **4**, eaau6915 (2018).
8. Cao, Y. et al. Correlated insulator behaviour at half-filling in magic-angle graphene superlattices. *Nature* **556**, 80–84 (2018).
9. Amin, K. R. & Bid, A. Effect of ambient on the resistance fluctuations of graphene. *Appl. Phys. Lett.* **106**, 183105 (2015).
10. Tiwari, P., Srivastav, S. K. & Bid, A. Electric-field-tunable valley zeeman effect in bilayer graphene heterostructures: Realization of the spin-orbit valve effect. *Phys. Rev. Lett.* **126**, 096801 (2021).
11. Avsar, A. et al. Spin-orbit proximity effect in graphene. *Nat. Commun.* **5**, 1–6 (2014).
12. Ingla-Aynés, J., Herling, F., Fabian, J., Hueso, L. E. & Casanova, F. Electrical control of valley-zeeman spin-orbit-coupling–induced spin precession at room temperature. *Phys. Rev. Lett.* **127**, 047202 (2021).
13. Sierra, J. F., Fabian, J., Kawakami, R. K., Roche, S. & Valenzuela, S. O. Van der waals heterostructures for spintronics andopto-spintronics. *Nat. Nanotechnol.* **16**, 856–868 (2021).
14. Zollner, K., Gmitra, M. & Fabian, J. Swapping exchange and spin-orbit coupling in 2d van der waals heterostructures. *Phys. Rev. Lett.* **125**, 196402 (2020).
15. Zollner, K. et al. Scattering-induced and highly tunable by gate damping-like spin-orbit torque in graphene doubly proximitized by two-dimensional magnet cr 2 ge 2 te 6 and monolayer ws 2. *Phys. Rev. Res.* **2**, 043057 (2020).
16. Safeer, C. et al. Room-temperature spin hall effect in graphene/mos2 van der waals heterostructures. *Nano Lett.* **19**, 1074–1082 (2019).
17. Cysne, T. P., Garcia, J. H., Rocha, A. R. & Rappoport, T. G. Quantum hall effect in graphene with interface-induced spin-orbit coupling. *Phys. Rev. B* **97**, 085413 (2018).
18. Garcia, J. H., Vila, M., Cummings, A. W. & Roche, S. Spin transport in graphene/transition metal dichalcogenide heterostructures. *Chem. Soc. Rev.* **47**, 3359–3379 (2018).
19. Wang, Z. et al. Strong interface-induced spin–orbit interaction in graphene on ws2. *Nat. Commun.* **6**, 1–7 (2015).
20. Avsar, A. et al. Colloquium: Spintronics in graphene and other two-dimensional materials. *Rev. Mod. Phys.* **92**, 021003 (2020).
21. Benítez, L. A. et al. Tunable room-temperature spin galvanic and spin hall effects in van der waals heterostructures. *Nat. Mater.* **19**, 170–175 (2020).
22. Weeks, C., Hu, J., Alicea, J., Franz, M. & Wu, R. Engineering a robust quantum spin hall state in graphene via adatom deposition. *Phys. Rev. X* **1**, 021001 (2011).
23. Balakrishnan, J., Koon, G. K. W., Jaiswal, M., Neto, A. C. & Özyilmaz, B. Colossal enhancement of spin–orbit coupling in weakly hydrogenated graphene. *Nat. Phys.* **9**, 284–287 (2013).
24. Gmitra, M. & Fabian, J. Proximity effects in bilayer graphene on monolayer wse$_2$: Field-effect spin valley locking, spin-orbit valve, and spin transistor. *Phys. Rev. Lett.* **119**, 146401 (2017).
25. Gmitra, M., Konschuh, S., Ertler, C., Ambrosch-Draxl, C. & Fabian, J. Band-structure topologies of graphene: Spin-orbit coupling effects from first principles. *Phys. Rev. B* **80**, 235431 (2009).
26. Yang, B. et al. Strong electron-hole symmetric rashba spin-orbit coupling in graphene/monolayer transition metal dichalcogenide heterostructures. *Phys. Rev. B* **96**, 041409 (2017).
27. Wang, Z. et al. Origin and magnitude of 'designer' spin-orbit interaction in graphene on semiconducting transition metal dichalcogenides. *Phys. Rev. X* **6**, 041020 (2016).
28. Xu, J., Zhu, T., Luo, Y. K., Lu, Y.-M. & Kawakami, R. K. Strong and tunable spin-lifetime anisotropy in dual-gated bilayer graphene. *Phys. Rev. Lett.* **121**, 127703 (2018).
29. Garcia, J. H., Cummings, A. W. & Roche, S. Spin hall effect and weak antilocalization in graphene/transition metal dichalcogenide heterostructures. *Nano Lett.* **17**, 5078–5083 (2017).
30. Han, W., Kawakami, R. K., Gmitra, M. & Fabian, J. Graphene spintronics. *Nat. Nanotechnol.* **9**, 794–807 (2014).
31. Wakamura, T. et al. Strong anisotropic spin-orbit interaction induced in graphene by monolayer ws 2. *Phys. Rev. Lett.* **120**, 106802 (2018).
32. Ghiasi, T. S., Ingla-Aynés, J., Kaverzin, A. A. & van Wees, B. J. Large proximity-induced spin lifetime anisotropy in transition-metal dichalcogenide/graphene heterostructures. *Nano Lett.* **17**, 7528–7532 (2017).
33. Offidani, M. & Ferreira, A. Microscopic theory of spin relaxation anisotropy in graphene with proximity-induced spin-orbit coupling. *Phys. Rev. B* **98**, 245408 (2018).
34. Luo, Y. K. et al. Opto-valleytronic spin injection in monolayer mos2/few-layer graphene hybrid spin valves. *Nano Lett.* **17**, 3877–3883 (2017).
35. Ghiasi, T. S., Kaverzin, A. A., Blah, P. J. & van Wees, B. J. Charge-to-spin conversion by the rashba–edelstein effect in two-dimensional van der waals heterostructures up to room temperature. *Nano Lett.* **19**, 5959–5966 (2019).
36. Kane, C. L. & Mele, E. J. Quantum spin hall effect in graphene. *Phys. Rev. Lett.* **95**, 226801 (2005).
37. Kane, C. L. & Mele, E. J. Z_2 topological order and the quantum spin hall effect. *Phys. Rev. Lett.* **95**, 146802 (2005).
38. Ilić, S., Meyer, J. S. & Houzet, M. Weak localization in transition metal dichalcogenide monolayers and their heterostructures with graphene. *Phys. Rev. B* **99**, 205407 (2019).
39. Gmitra, M., Kochan, D., Högl, P. & Fabian, J. Trivial and inverted dirac bands and the emergence of quantum spin hall states in graphene on transition-metal dichalcogenides. *Phys. Rev. B* **93**, 155104 (2016).
40. Khoo, J. Y., Morpurgo, A. F. & Levitov, L. On-demand spin-orbit interaction from which-layer tunability in bilayer graphene. *Nano Lett.* **17**, 7003–7008 (2017).
41. Cummings, A. W., Garcia, J. H., Fabian, J. & Roche, S. Giant spin lifetime anisotropy in graphene induced by proximity effects. *Phys. Rev. Lett.* **119**, 206601 (2017).
42. Gmitra, M. & Fabian, J. Graphene on transition-metal dichalcogenides: A platform for proximity spin-orbit physics and optospintronics. *Phys. Rev. B* **92**, 155403 (2015).
43. Island, J. et al. Spin–orbit-driven band inversion in bilayer graphene by the van der waals proximity effect. *Nature* **571**, 85–89 (2019).
44. Omar, S. & van Wees, B. J. Spin transport in high-mobility graphene on ws$_2$ substrate with electric-field tunable proximity spin-orbit interaction. *Phys. Rev. B* **97**, 045414 (2018).
45. Offidani, M., Milletarì, M., Raimondi, R. & Ferreira, A. Optimal charge-to-spin conversion in graphene on transition-metal dichalcogenides. *Phys. Rev. Lett.* **119**, 196801 (2017).
46. Leutenantsmeyer, J. C., Ingla-Aynés, J., Fabian, J. & van Wees, B. J. Observation of spin-valley-coupling-induced large spin-lifetime anisotropy in bilayer graphene. *Phys. Rev. Lett.* **121**, 127702 (2018).
47. Benítez, L. A. et al. Strongly anisotropic spin relaxation in graphene–transition metal dichalcogenide heterostructures at room temperature. *Nat. Phys.* **14**, 303–308 (2018).
48. Zihlmann, S. et al. Large spin relaxation anisotropy and valley-zeeman spin-orbit coupling in wse$_2$/graphene/h-bn heterostructures. *Phys. Rev. B* **97**, 075434 (2018).
49. Pizzocchero, F. et al. The hot pick-up technique for batch assembly of van der waals heterostructures. *Nat. Commun.* **7**, 1–10 (2016).
50. Wang, L. et al. One-dimensional electrical contact to a two-dimensional material. *Science* **342**, 614–617 (2013).
51. Novoselov, K. S. et al. Two-dimensional gas of massless dirac fermions in graphene. *Nature* **438**, 197–200 (2005).
52. Küppersbusch, C. & Fritz, L. Modifications of the lifshitz-kosevich formula in two-dimensional dirac systems. *Phys. Rev. B* **96**, 205410 (2017).
53. Lifshitz, I. & Kosevich, A. Theory of magnetic susceptibility in metals at low temperatures. *Sov. Phys. JETP* **2**, 636–645 (1956).
54. Neto, A. C., Guinea, F., Peres, N. M., Novoselov, K. S. & Geim, A. K. The electronic properties of graphene. *Rev. Mod. Phys.* **81**, 109 (2009).
55. Hwang, C. et al. Fermi velocity engineering in graphene by substrate modification. *Sci. Rep.* **2**, 1–4 (2012).

AUTHOR CONTRIBUTIONS
P.T. and A.B. conceived the idea of this research. P.T. and D.S.N. fabricated the devices; P.T., M.K.J., and A.B. performed the measurements; A.U. and D.S. provided theoretical support; K.W. and T.T. grew the material; P.T., M.K.J., and A.B. did the experimental data analysis. P.T., A.U., and A.B. co-wrote the manuscript. All authors discussed the results and commented on the manuscript.

COMPETING INTERESTS
The authors declare no competing interests.

ADDITIONAL INFORMATION
Supplementary information The online version contains supplementary material available at https://doi.org/10.1038/s41699-022-00348-y.

Correspondence and requests for materials should be addressed to Aveek Bid.

Reprints and permission information is available at http://www.nature.com/reprints